

the system to change basin. Our results suggest that comparable constraints must characterize those regions of configuration space explored at different temperatures in a fixed landscape, and regions explored at a given temperature in a family of energy landscapes resulting from either covalent-bond formation or volume reduction. Thus, the general applicability of equation (1) evidently rests on universal properties in the organization of energy landscapes, and microscopic diversity must be absorbed into statistical properties, possibly governed by limit theorems. Manifestations of that might be looked for in simulation studies.

Indeed, a glass can be obtained both as a result only of compression, and as a result only of reaction, as the underlying evolution of configurational restrictions turns out to be similar. Nevertheless, the mechanism of disappearance of accessible minima is different in the two cases. Whereas a volume change involves a simultaneous modification of the interactions in all parts of the system and alters everywhere its configuration space, the formation of any new covalent bond does not entail a long-range modification of the energy landscape. The resulting landscapes may be topologically different. In this connection, we note that kinetic fragility (which has a thermodynamic^{16,28} measure in the rapidity of change with T of configurational entropy) is likely to reflect such difference; indeed, the kinetic fragility is expected from equation (2) to become lower with increasing α , whereas it is found to become higher with decreasing volume¹⁶. □

Received 7 August; accepted 23 October 2002; doi:10.1038/nature01261.

- Debenedetti, P. G. *Metastable Liquids. Concepts and Principles* (Princeton Univ. Press, Princeton, 1996).
- Deng, Y. & Martin, C. Analysis of the cure-dependent dielectric relaxation behavior of an epoxy resin. *J. Polym. Sci. B* **32**, 2115–2125 (1994).
- Cassettari, M., Salvetti, G., Tombari, E., Veronesi, S. & Johari, G. P. Dielectrics and thermodynamics of a macromolecule's growth. *J. Non-Cryst. Solids* **172–174**, 554–561 (1994).
- Casalini, R., Corezzi, S., Fioretto, D., Livi, A. & Rolla, P. A. Unified dielectric description of the dynamics of polymeric systems undergoing either thermal or chemical vitrification. *Chem. Phys. Lett.* **258**, 470–476 (1996).
- Tombari, E., Ferrari, C., Salvetti, G. & Johari, G. P. Molecular dynamics during linear chain polymerization from real-time dielectric spectrometry and calorimetry. *J. Phys. Condens. Matter* **9**, 7017–7037 (1997).
- Johari, G. P., Ferrari, C., Tombari, E. & Salvetti, G. Temperature modulation effects on a material's properties: Thermodynamics and dielectric relaxation during polymerization. *J. Chem. Phys.* **110**, 11592–11598 (1999).
- Gallone, G., Capaccioli, S., Levita, G., Rolla, P. A. & Corezzi, S. Dielectric analysis of the linear polymerization of an epoxy resin. *Polym. Int.* **50**, 545–551 (2001).
- Parthun, M. G. & Johari, G. P. Dielectric spectroscopy of a polymerizing liquid and the evolution of molecular dynamics with increase in the number of covalent bonds. *J. Chem. Phys.* **103**, 440–450 (1995).
- Johari, G. P., Ferrari, C., Salvetti, G. & Tombari, E. Physico-chemical aspects of dielectric and thermodynamic changes during high-temperature polymerization and their technical use. *Phys. Chem. Chem. Phys.* **1**, 2997–3005 (1999).
- Adam, G. & Gibbs, J. H. On the temperature dependence of cooperative relaxation properties in glass-forming liquids. *J. Chem. Phys.* **43**, 139–146 (1965).
- Xia, X. & Wolynes, P. G. Fragilities of liquids predicted from the random first order transition theory of glasses. *Proc. Natl Acad. Sci. USA* **97**, 2990–2994 (2000).
- Richert, R. & Angell, C. A. Dynamics of glassforming liquids. V: On the link between molecular dynamics and configurational entropy. *J. Chem. Phys.* **108**, 9016–9026 (1998).
- Casalini, R., Capaccioli, S., Lucchesi, M., Rolla, P. A. & Corezzi, S. Pressure dependence of structural relaxation time in terms of the Adam-Gibbs model. *Phys. Rev. E* **63**, 031207 (2001).
- Casalini, R. *et al.* Effect of pressure on the dynamics of glass formers. *Phys. Rev. E* **64**, 041504 (2001).
- Scala, A., Starr, F. W., La Nave, E., Sciortino, F. & Stanley, H. E. Configurational entropy and diffusivity of supercooled water. *Nature* **406**, 166–169 (2000).
- Sastry, S. The relationship between fragility, configurational entropy and the potential energy landscape of glass-forming liquids. *Nature* **409**, 164–167 (2001).
- Matsuoka, S., Quan, X., Bair, H. E. & Boyle, D. J. A model for the curing reaction of epoxy resins. *Macromolecules* **22**, 4093–4098 (1989).
- Young, R. J. & Lovell, P. A. *Introduction to Polymers* (Chapman and Hall, New York, 1991).
- Macosko, C. W. & Miller, D. R. A new derivation of average molecular weights of nonlinear polymers. *Macromolecules* **9**, 199–206 (1976).
- Kauzmann, W. The nature of the glassy state and the behavior of liquids at low temperatures. *Chem. Rev.* **43**, 219–256 (1948).
- Vogel, H. Temperature dependence of viscosity of melts. *Phys. Z.* **22**, 645–646 (1921).
- Angell, C. A. Relaxation in liquids, polymers and plastic crystals—strong/fragile patterns and problems. *J. Non-Cryst. Solids* **131–133**, 13–31 (1991).
- Stillinger, F. H. A topographic view of supercooled liquids and glass formation. *Science* **267**, 1935–1939 (1995).
- Sastry, S., Debenedetti, P. G. & Stillinger, F. H. Signatures of distinct dynamical regimes in the energy landscape of a glass-forming liquid. *Nature* **393**, 554–557 (1998).
- Debenedetti, P. G. & Stillinger, F. H. Supercooled liquids and the glass transition. *Nature* **410**, 259–267 (2001).

- La Nave, E., Mossa, S. & Sciortino, F. Potential energy landscape equation of state. *Phys. Rev. Lett.* **88**, 225701 (2002).
- Kumar, S. K. & Douglas, J. F. Gelation in physically associating polymer solutions. *Phys. Rev. Lett.* **87**, 188301 (2001).
- Martinez, L.-M. & Angell, C. A. A thermodynamic connection to the fragility of glass-forming liquids. *Nature* **410**, 663–667 (2001).
- Luňák, S. & Dušek, K. Curing of epoxy resins. II. Curing of bisphenol A diglycidyl ether with diamines. *J. Polym. Sci. Polym. Symp. Edn* **53**, 45–55 (1975).

Acknowledgements We thank G. Gallone and S. Capaccioli for providing dielectric measurements on EPON828/EDA 1:1 and EPON828/BAM 1:1 systems, and L. Comez, P. Grigolini, S. Mossa, G. Ruocco, A. Scala and G. Socino for comments on the manuscript. We particularly thank F. Sciortino for assistance.

Competing interests statement The authors declare that they have no competing financial interests.

Correspondence and requests for materials should be addressed to S.C. (e-mail: Silvia.Corezzi@fisica.unipg.it).

Decreased stability of methane hydrates in marine sediments owing to phase-boundary roughness

W. T. Wood*, J. F. Gettrust*, N. R. Chapman†, G. D. Spence‡ & R. D. Hyndman‡

* US Naval Research Laboratory, Stennis Space Center, Mississippi 39529, USA

† University of Victoria, Victoria, British Columbia V8W 3P6, Canada

‡ Pacific Geosciences Center, Sydney, British Columbia V8L 4B2, Canada

Below water depths of about 300 metres, pressure and temperature conditions cause methane to form ice-like crystals of methane hydrate¹. Marine deposits of methane hydrate are estimated to be large, amassing about 10,000 gigatonnes of carbon², and are thought to be important to global change^{3,4} and seafloor stability^{5,6}, as well as representing a potentially exploitable energy resource⁷. The extent of these deposits can usually be inferred from seismic imaging, in which the base of the methane hydrate stability zone is frequently identifiable as a smooth reflector that runs parallel to the sea floor. Here, using high-resolution seismic sections of seafloor sediments in the Cascadia margin off the coast of Vancouver Island, Canada, we observe lateral variations in the base of the hydrate stability zone, including gas-rich vertical intrusions into the hydrate stability zone. We suggest that these vertical intrusions are associated with upward flow of warmer fluids. Therefore, where seafloor fluid expulsion and methane hydrate deposits coincide, the base of the hydrate stability zone might exhibit significant roughness and increased surface area. Increased area implies that significantly more methane hydrate lies close to being unstable and hence closer to dissociation in the event of a lowering of pressure due to sea-level fall.

The data we present were acquired with a unique seismic system (deep-towed acoustic/geophysics system; DTAGS⁸) that can be towed close to the sea floor, resulting in a reduced Fresnel zone (lateral area over which a reflected signal is averaged) and increased lateral resolution. Also, because DTAGS is operated at 250–650 Hz, rather than 10–80 Hz, the resulting vertical and lateral resolutions are almost an order of magnitude greater than conventional seismic systems⁹. Deployment of DTAGS on the accretionary prism of the Cascadia margin, a region known for a strong bottom-simulating reflector (BSR), and widespread evidence of fluid flux and methane hydrate^{10–12}, resulted in some intriguing observations that are

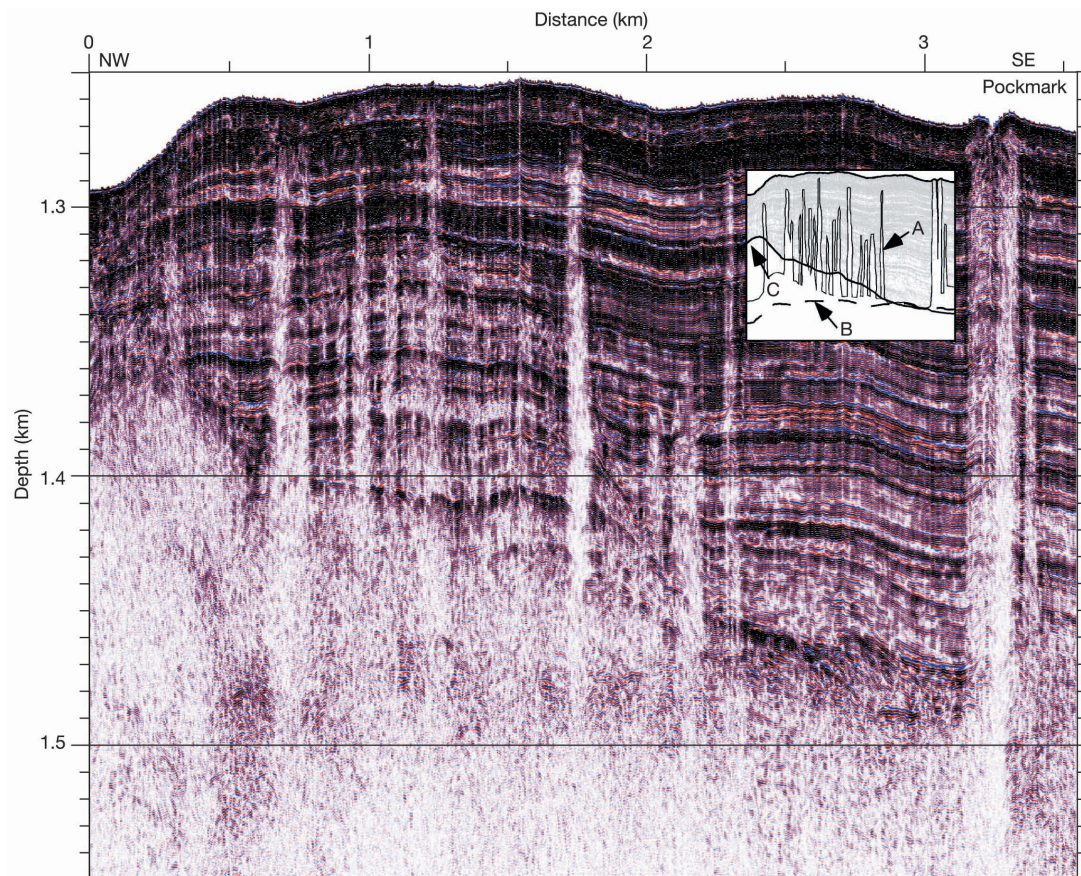


Figure 1 High-resolution seismic images of the hydrate stability zone (upper 220 m of sediment) on the Cascadia margin about halfway between Ocean Drilling Program sites 889 and 890 (ref. 10). Vertically oriented gas accumulations (curve A, inset) scatter and absorb the incoming energy, resulting in little acoustic energy returning upward to be recorded. Gas accumulations conformable with short pieces of near-horizontal strata

(curve B, inset) within the highly deformed accreted sediments (below curve C, inset) greatly enhance the energy coherently reflected upward. The presence of gas within the hydrate stability zone suggests that the zone might have been perturbed by warm fluids, occasionally resulting in a seafloor pockmark. These perturbations significantly increase the surface area and subsequently the volatility of the methane hydrate reservoir.

apparent in Fig. 1. The sediment column here exhibits vertical zones of little to no coherently reflected seismic energy (wipeouts), slightly wider at the bottom than at the top (Fig. 1 inset, fine curve A), occasionally intersecting the sea floor. At least some of the intersections are associated with pockmarks (Fig. 1). In addition, instead

of the strong BSR seen in conventional seismic data throughout this area¹¹, we see a diffuse cloud of short reflection segments becoming more intense when proximal to the wipeouts (Fig. 1 inset, curve B). Because BSRs are caused by the coherent reflectivity of methane gas accumulation at (or just below¹³) the depth of the base of gas

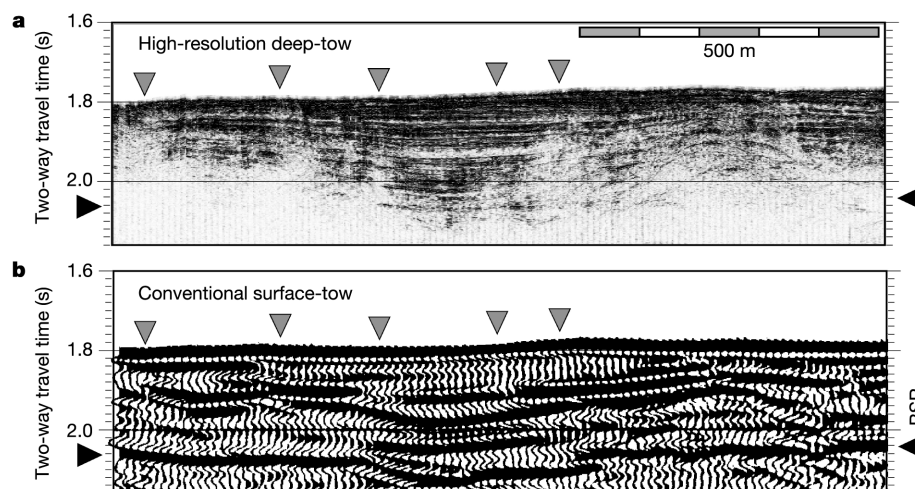


Figure 2 Two views of the same portion of the methane hydrate stability zone. Areas of reduced amplitude due to fine-scale flux conduits (grey arrowheads) are apparent in the

DTAGS data (a) but not in the airgun data (b, line 89-08 from ref. 10), whereas a coherent BSR (black arrowheads) is apparent in the airgun data but not the DTAGS data.

hydrate stability (BGHS), and are sensitive to fluid and heat flux¹, the wipeouts and perturbations imaged here are probably indicators of fine-scale fluid flux through the upper sea floor.

The level of detail in these images can be appreciated better where both DTAGS and conventional data are exactly coincident and displayed at the same scale, as in Fig. 2. The higher frequencies and smaller Fresnel zone of DTAGS allows the identification of the narrow wipeouts (grey arrowheads in Fig. 2) but do not have the penetration of conventional systems, especially in the more indurated accretionary wedge sediments that contain the BSR (black arrowheads in Fig. 2). It is also significant that the shorter wavelengths associated with higher frequencies require increased accuracy in source and receiver geometry¹², which is extremely difficult to achieve in any marine experiment. The optimal DTAGS images displayed here require an increased effort in data processing over that of the conventional seismic image.

Even with the higher-resolution images, the exact geologic cause of the wipeouts is ambiguous; we are certain only that the seismic energy is not coherently reflected back to the receiver array. The energy can be absorbed (for example, by gas) or scattered, perhaps by sub-metre-scale unevenly distributed accumulations of gas, methane hydrate or calcium carbonate (CaCO₃), or by stratal disruption from intense fluid flux. However, the seafloor pockmarks and carbonate mineralization associated with some wipeouts are clear indicators (if only qualitative) of upward fluid flux and, by inference, heat flux.

Several factors lead us to propose that the wipeouts are caused by gas, the outline of which coincides with columnar perturbations in the BGHS. First, the wipeouts are strikingly similar in size and character to 'gas chimneys'^{214,15}, vertically oriented accumulations of gas which have been seen in conventional seismic data from several parts of the world, and in water depths too shallow to sustain

methane hydrate¹⁶. In addition, localized heat flux mediated by advecting fluid implies that the pressure–temperature boundary defining the BGHS is perturbed upwards from the regional average at least mildly, and perhaps quite severely, especially where the wipeout is coincident with a seafloor pockmark, creating a region within which methane hydrate dissociates and releases gas. Because methane hydrate at depth is warmer and more easily dissociated than methane hydrate near the sea floor, we expect the perturbation to broaden with depth, which is consistent with the observed outline of many of the wipeouts.

This interpretation of the wipeouts as gas chimneys is also consistent with preliminary finite element modelling (SUTRA¹⁷), using actual measurements of temperature, pressure and physical properties from this area¹⁰, and measured properties of methane hydrate stability¹⁸. The wipeout shown in Fig. 3 is an expanded view of the wipeout located at 2.3 km in Fig. 1, and was modelled in three dimensions assuming radial symmetry about a vertical zone with a permeability three orders of magnitude greater than the surrounding sediments (see Methods for details). Every modelling attempt resulted in a flared base to the stability boundary (dashed line in Fig. 3), which is consistent with the outline of this and most other wipeouts. The absolute height and width of the perturbation depend on conduit permeability and on temporal functions of fluid flux rates and temperature, none of which are well constrained on the scale of metres to tens of metres, but the results demonstrate

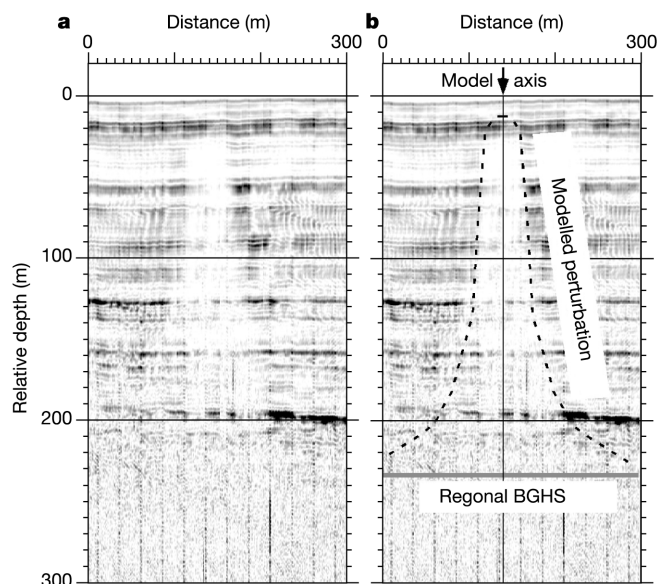


Figure 3 Finite element modelling results for heat and fluid flux of the wipeout at 2.3 km in Fig. 1. **a**, This wipeout is a contrast in seismic reflection amplitude emphasized here by displaying the instantaneous amplitude of the signal (light and dark shades are low and high amplitudes, respectively) and using relatively low gain. **b**, Finite element modelling of heat and fluid flux was performed assuming radial symmetry about a vertical flux conduit axially located within the wipeout. After many tens of thousands of years of model time the temperature field stabilized and the resulting perturbation (dashed line) of the regional stability boundary (grey horizontal line) was calculated. The downward flare of the perturbation is consistent with the boundary of this and most other wipeouts.

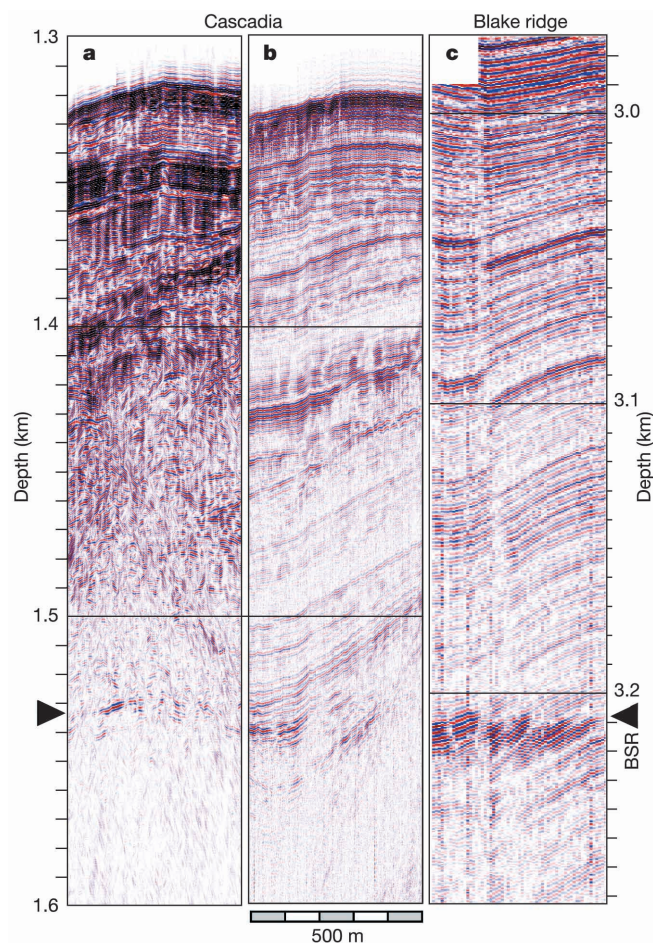


Figure 4 A comparison of BSRs. Where gas accumulations are small relative to the ensconifying wavelength and the Fresnel zone (**a**), the BSR appears as a single reflection. Where the gas accumulation is larger, and strata are resolvable (**b**, **c**), the BSR is a reflective zone of enhanced reflectivity conformable with the strata.

that, in areas of fluid and heat flux, methane gas can exist well inside the regional hydrate stability zone.

Thus in our interpretation the chimneys represent a significantly increased surface area of the BGHS, increasing the responsiveness of the methane hydrate reservoir to methane release or sequestration in the event of sea-level fall or rise, respectively. When plotted with no vertical exaggeration, the interpreted BGHS (curve A in Fig. 1 inset) is about 1.64 times as long as the expected, or unperturbed, BGHS (curve B in Fig. 1 inset). If we assume that the distribution of chimneys in the surveyed area is the same across the section in Fig. 1 as it is within the section, we find anything from a 0.5-fold to a 3.0-fold increase in the surface area of the phase boundary (depending on the interpretation of the wipeout boundary) and therefore the volatility of the sequestered hydrate. The chimneys are also important from a purely practical standpoint, representing remotely detectable fluid flux conduits that are probably associated with increased hydrate concentrations close to the stability boundary, and are of primary importance in any physical, chemical, biological or industrial study of methane hydrates^{1,7,19}.

The other phenomenon observed in the DTAGS data also relates to the roughness of the BGHS, but at a much smaller scale. The data also reveal BSRs with a significantly different character from that of the strong, reversed-polarity, strata-crossing reflection frequently observed in surface-tow seismic data such as those in Fig. 2. Published modelling of a wide range of data including conventional and DTAGS data shows that much of the reduced amplitude can be explained by a vertical velocity gradient that is gentle (less reflective) for high-frequency data and sharper (more reflective) for low-frequency data¹².

The new images do not refute the gradient model, but they suggest that lateral variability is likely to be a significant factor in the appearance of the BSR. The data indicate that anywhere the strata containing the BSR are resolvable, the BSR appears only as an upper extent of reflective sediments below and is not an unconformable reflection. Only when the spatial scale of the sedimentary structure falls below the lateral resolution of the seismic system in use does the BSR seem to cut across local strata. This is consistent with a BSR caused by localized accumulations of gas preferentially occupying more porous strata, thereby merely enhancing the existing reflectivity instead of creating an additional reflector. In contrast to the much larger-scale chimneys, the BGHS need not be perturbed to exhibit this character.

An example of this lateral variability is shown in Fig. 4b, where the BSR is more parallel to surrounding sediments at the left than to those at the right, giving the BSR a more continuous appearance on the left and a shingled appearance on the right. A very similar transition is seen in Fig. 4c in DTAGS data acquired on the Atlantic side of the continent over a large sediment drift, the Blake Ridge, near Ocean Drilling Program site 997, another region known for a prominent BSR and hydrate accumulations^{20,21}. Again, the BSR undergoes a transition from parallel to shingled from left to right, although the section from the Blake ridge exhibits a sharper distinction between the gas-free sediments above and the gas-charged sediments below. Geologically and hydrologically, the two settings are quite different except that both areas exhibit conspicuous BSRs and are made up of fine-grained sediments typical of continental margins, where most methane hydrates are suspected to occur².

In areas of greater sediment deformation, such as the accreted sediments of the Cascadia margin, no sedimentary strata are resolvable, and the short coherent segments of reflections that we see in the DTAGS data (the diffuse cloud in Fig. 1, or the intermittent single reflector in Fig. 4a) might well be laterally oriented assemblages of sub-metre-scale accumulations that appear coherent only when averaged over the first Fresnel zone of the ensonifying seismic wave. This is analogous to the individually resolvable segments in Fig. 4c seeming coherent in lower-frequency surface-tow data²¹.

Last, the BSR in the DTAGS data is most conspicuous immediately adjacent to chimneys (Fig. 1) and to some extent the faults (Fig. 4). Note the thicker region of intense reflections near the bases of the more prominent chimneys in Fig. 1. This is consistent with fluid flux focused at the chimneys enriching the surrounding sediment with methane. Within the wipeout we expect the free gas to be oriented along the near-vertical flux conduits, effectively scattering the seismic signal; below the BGHS adjacent to the wipeout we expect near-horizontally oriented free gas, occupying pore space within preferentially permeable and porous strata, and enhancing their coherent seismic reflectivity (the BSR). Although there is no direct evidence, we would also expect an increased concentration of gas hydrate filling pores immediately adjacent to the wipeout above the regional BGHS, mimicking the increased free gas below the regional BGHS.

The high-resolution images of the methane hydrate stability zone and its lower boundary depicted here support a model of hydrate distribution strongly affected, if not dominated, by focused vertical fluid flux. This complicates the estimation of methane hydrate quantities obtained through extrapolation from a single drill hole, and indicates that of the estimated 10,000 gigatonnes of carbon sequestered in methane hydrates, a significantly greater portion might lie closer to the stability boundary than if it were evenly distributed throughout an unperturbed stability zone. □

Methods

Preliminary modelling of BGHS perturbation from advective heat flux was performed with the finite element program SUTRA¹⁶. Figure 3 shows the modelling result from one of the seismic wipeouts from the Cascadia margin. A three-dimensional result was obtained with a two-dimensional model by assuming radial symmetry about a vertical flux conduit. Each of the 30 × 30 elements used represents a region 10 m in depth by 10 m outwards from the conduit. The conduit was modelled by setting the hydraulic conductivity of the inner two columns to be three orders of magnitude greater than in the surrounding sediments.

Appropriate initial and boundary conditions as well as sediment and fluid properties used in the SUTRA modelling were based on published measurements made at Ocean Drilling Program sites 889 and 890 (ref. 10) only a few kilometres away from the modelled wipeout and in the same geologic setting. Fraction porosity (ϕ), pressure in MPa (P) and temperature in °C (T) were all given initial conditions that were linear functions of depth in metres, z (positive downwards), namely $\phi(z) = 0.63 - 0.0005z$, $P(z) = 13.0585 + 0.012054z$ and $T(z) = 2.6 + 0.0545z$. The pressure and temperature on the model boundaries, that is, the top of the model (sea floor), base of the model (at 300 m below the sea floor) and outer edge of the model (300 m radius from the conduit) were held fixed throughout the simulation at their initial values. The physical properties of the fluid and solid used in the model were respectively: compressibility, 4.9×10^{-10} and 0.0 Pa^{-1} ; specific heat, 4,182 and 4,840 $\text{J kg}^{-1} \text{ K}^{-1}$; thermal conductivity, 0.528 and 1.516 $\text{W m}^{-1} \text{ K}^{-1}$; and density, 1.035 and 2.65 g cm^{-3} . The value of the dispersion coefficient used in the model was 5 in all directions. In the conduit, vertical and lateral hydraulic conductivity are both $10^{-13} \text{ m s}^{-1}$; in the surrounding sediment, vertical and lateral hydraulic conductivities are 10^{-17} and $10^{-16} \text{ m s}^{-1}$, respectively.

The model was allowed to proceed to 10,000 years model time, when the change between subsequent 100-year time steps was negligible. The constant-pressure boundary at the base of the model allowed greater fluid and heat flux through the high-permeability conduit than through the surrounding sediment, thus perturbing the thermal profile. The equilibrium thermal profile provided by SUTRA was then used with the assumed pressure profile and a measured hydrate stability curve¹⁸ to determine the perturbation (dashed line in Fig. 3) of the regional BGHS (grey line in Fig. 3). Although several key modelling conditions (such as pressure and hydraulic conductivity) are poorly constrained, the characteristic shape of the thermal perturbation is, as expected, wider at the base than at the top. Although exhaustive testing has not yet been performed, every model run exhibited a downward flare in the BGHS, which is consistent with the observed profile of most of the wipeouts.

Received 20 May; accepted 28 October 2002; doi:10.1038/nature01263.

1. Paull, C. K. & Dillon, W. P. (eds) *Natural Gas Hydrates: Occurrence, Distribution, and Dynamics* AGU Monograph no. 124 (American Geophysical Union, Washington DC, 2001).
2. Kvenvolden, K. A. & Lorenson, T. D. *Natural Gas Hydrates: Occurrence, Distribution, and Dynamics* AGU Monograph no. 124 (eds Paull, C. K. & Dillon, W. P.) 3–18 (American Geophysical Union, Washington DC, 2001).
3. Paull, C. K., Ussler, W. & Dillon, W. P. Is the extent of glaciation limited by marine gas-hydrates? *Geophys. Res. Lett.* **18**, 432–434 (1991).
4. Dickens, G. R., Castillo, M. M. & Walker, J. C. G. A blast of gas in the latest Paleocene: simulating first-order effects of massive dissociation of oceanic methane hydrate. *Geology* **25**, 259–262 (1997).
5. Paull, C. K., Buelow, W., Ussler, W. & Borowski, W. S. Increased continental-margin slumping frequency during sea-level lowstands above gas hydrate-bearing sediments. *Geology* **24**, 143–146 (1996).

6. Booth, J. S., Winters, W. J. & Dillon, W. P. Circumstantial evidence of gas hydrate and slope failure associations on US Atlantic continental margin. *Ann. N.Y. Acad. Sci.* **75**, 487–489 (1994).
7. Collett, T. S. & Kuuskraa, V. A. Hydrates contain vast store of world gas resources. *Oil Gas J.* 11 May, 90–95 (1998).
8. Gettrust, J. F., Ross, J. H. & Rowe, M. M. Development of a low frequency, deep-tow geacoustics system. *Sea Technol.* **32**, 23–32 (1991).
9. Wood, W. T. & Gettrust, J. F. *Natural Gas Hydrates: Occurrence, Distribution, and Dynamics* AGU Monograph no. 124 (eds Paull, C. K. & Dillon, W. P.) 165–178 (American Geophysical Union, Washington DC, 2001).
10. Westbrook, G. K., Carson, B., Musgrave, R. J. & Suess, E. *Proc. ODP Init. Rep.* **146** (1994).
11. Hyndman, R. D. & Spence, G. D. A seismic study of methane hydrate marine bottom-simulating reflectors. *J. Geophys. Res.* **97**, 6683–6698 (1992).
12. Chapman, N. R. et al. High-resolution, deep-towed, multichannel seismic survey of deep-sea gas hydrates off western Canada. *Geophysics* **67**, 1038–1047 (2002).
13. Xu, W. & Ruppel, C. Predicting the occurrence, distribution, and evolution of methane gas hydrate in porous marine sediments. *J. Geophys. Res.* **104**, 5081–5095 (1999).
14. Heggland, R., Meldahl, P., de Groot, P. & Aminzadeh, F. Chimney cube unravels subsurface. *Am. Oil Gas Reporter* 78–83 (February 2000).
15. Meldahl, P., Heggland, R., Bril, B. & de Groot, P. Identifying faults and gas chimneys using multiattributes and neural networks. *Leading Edge* **20**, 474–482 (2001).
16. Hovland, M. & Judd, G. *Seabed Pockmarks and Seepages* 181 (Graham & Trotman, London, 1988).
17. Voss, C. I. A finite element simulation model for saturated and unsaturated, fluid-density-dependent ground-water flow with energy transport or chemically reactive single species solute transport (USGS Water Resources Investigations Report 84–4369, 1984).
18. Brown, K. M., Bangs, N. L., Froelich, P. N. & Kvenvolden, K. A. The nature, distribution and origin of gas hydrate in the Chile Triple Junction region. *Earth Planet. Sci. Lett.* **139**, 471–483 (1996).
19. Fisher, C. R. et al. Methane ice worms: *Hesiocaea methanicola* colonizing fossil fuel reserves. *Naturwissenschaften* **87**, 184–187 (2000).
20. Paull, C. K., Matsumoto, R. & Wallace, P. *Proc. ODP Init. Rep.* **164** (1996).
21. Korenaga, J., Holbrook, W. S., Singh, S. C. & Minshall, T. A. Natural gas hydrates on the southeast U.S. margin: Constraints from full waveform and travel time inversions of wide angle seismic data. *J. Geophys. Res.* **102**, 15345–15365 (1997).

Acknowledgements We thank C. Voss for advice on finite element modelling.

Competing interests statement The authors declare that they have no competing financial interests.

Correspondence and requests for materials should be addressed to W.W. (e-mail: warren.wood@nrlssc.navy.mil).

Unconventional lift-generating mechanisms in free-flying butterflies

R. B. Srygley & A. L. R. Thomas

Department of Zoology, University of Oxford, South Parks Road, Oxford OX1 3PS, UK

Flying insects generate forces that are too large to be accounted for by conventional steady-state aerodynamics^{1,2}. To investigate these mechanisms of force generation, we trained red admiral butterflies, *Vanessa atalanta*, to fly freely to and from artificial flowers in a wind tunnel, and used high-resolution, smoke-wire flow visualizations to obtain qualitative, high-speed digital images of the air flow around their wings. The images show that free-flying butterflies use a variety of unconventional aerodynamic mechanisms to generate force: wake capture³, two different types of leading-edge vortex^{3–7}, active and inactive upstrokes⁸, in addition to the use of rotational mechanisms³ and the Weis-Fogh ‘clap-and-fling’ mechanism^{9–12}. Free-flying butterflies often used different aerodynamic mechanisms in successive strokes. There seems to be no one ‘key’ to insect flight, instead insects rely on a wide array of aerodynamic mechanisms to take off, manoeuvre, maintain steady flight, and for landing.

The lift-generating forces that are created by insects during flight are greater than conventional aerodynamic mechanisms allow. Recent experiments with tethered hawkmoths, and with large-scale mechanical flapping models, have successfully replicated some of the force-generating abilities of insects^{3–7}. Leading-edge

vortices form over the wings of both hawkmoths and models during the downstroke. A vortex held above a wing has long been known to be capable of generating lift^{2,13–19}. A transient leading-edge vortex can be formed by sudden changes in flow velocity²⁰ or pitch²¹, and aerodynamic experiments in unsteady flows have shown that at its peak, the vortex can increase the lift coefficient markedly above the steady-state value for a given aerofoil^{2,20,21}. Studies with model insects^{3,6,7} suggest that leading-edge vortices can be quite stable over model insect wings, and may produce a twofold increase in lift. There are at least two other aerodynamic mechanisms involved in insect flight: one associated with wing rotation^{1,3,7} and another associated with wake capture^{3,7}; however, until now the flow features associated with wake capture and rotational mechanisms have not been identified in real insects, even in tethered flight.

There are also qualitative differences between the published structures of the leading-edge vortices formed over two flapper models^{3,5–7}. The flow field around the hawkmoth flapper model is apparently analogous to the leading-edge vortices over delta wings, with vortex stability maintained by the removal of vorticity through a spanwise (base of the wing to the wing-tip) axial flow along the vortex cores^{5,6}. However, chordwise fences on the wings of the *Drosophila* flapper model stopped spanwise flow but not the leading edge vortex, which even increased in size and strength³. Flow visualization experiments with tethered hawkmoths showed leading-edge vortices^{5,6}, but with insufficient resolution to reveal the internal structure. Furthermore the hawkmoths were tethered, and although an insect on a tether may flap its wings, this is not real flight.

To overcome the problems associated with tethered insects, we used a high-resolution, flow visualization system to examine the details of the field of air flow around the wings of free-flying butterflies (*Vanessa atalanta*). To describe the topology of the different three-dimensional separated flows that free-flying butterflies produce, we used critical point concepts^{22–27}.

The butterflies in our experiments used all of the unsteady aerodynamic mechanisms that have been proposed. They switch between mechanisms freely—often using completely different mechanisms on successive wing strokes—and are able to choose different aerodynamic mechanisms to suit different flight behaviours. Visualizations of air flow in free flight show that the fluttering of butterflies is not a random, erratic wandering, but results from a mastery of wide array of aerodynamic mechanisms available to free-flying insects.

Figure 1a shows the typical flow field over the midline of a butterfly during a downstroke. The flow is clearly not of the type described in previous studies^{3,5,7} and of that shown in Fig. 1b. Instead, an open U-shaped separation exists above the insect with a free-slip critical point (saddle) above the midline. This distinct pattern of leading-edge vortex flow has a nodal point of attachment on the midline. Lines of attachment run from this nodal-point along the undersurface of the wings to the wing-tips; there is a saddle point of separation on the top surface of the body from which lines of separation run to the wing-tips close to, or along, the leading edge. There is a free-slip critical point (saddle) above the midline, and the leading-edge vortices extend out from this free-slip critical point along the wings and on into the wing-tip vortices (with which they are continuous). The leading-edge vortices are not conical or spiral in any of our images, but are of approximately constant diameter, and if there is any spanwise flow it is too weak to be detected. In such images, spanwise flow would appear as a distortion of the curved smoke streams passing round the leading-edge vortex, with streams nearer the centre of the leading-edge vortex being pulled out towards the wing-tips or even turning to flow along the wings towards the wing-tips. This sort of distortion is not visible in any of our flow visualizations of *V. atalanta*. Re-attachment occurs either at a nodal point of attachment on the rear of the body from which lines of attachment run to the wing-tips, or at a free-slip